An experimental-numerical method to determine the work-hardening of anisotropic ductile materials at large strains

M. Khadyko[1,*], S. Dumoulin[2], T. Børvik[1] and O.S. Hopperstad[1]

[1] *Structural Impact Laboratory (SIMLab), Centre for Research-based Innovation, Department of Structural Engineering, Norwegian University of Science and Technology, NO-7491 Trondheim, Norway*

[2]*SINTEF Materials & Chemistry, NO-7465 Trondheim, Norway*

Abstract

The determination of work hardening for ductile materials at large strains is difficult to perform in the framework of usual tensile tests because of the geometrical instability and necking in the specimen at relatively low strains. In this study we propose a combination of experimental and numerical techniques to overcome this difficulty. Extruded aluminium alloys are used as a case since they exhibit marked plastic anisotropy. In the experiments, the minimum diameters of the axisymmetric tensile specimen in two normal directions are measured at high frequency by a laser gauge in the necking area together with the corresponding force, and the true stress-strain curve is found. The anisotropy of the material is determined from its crystallographic texture using the crystal plasticity theory. This data is used to represent the specimen by a 3D finite element model with phenomenological anisotropic plasticity. The experimental true stress-strain curve is then used as a target curve in an optimization procedure for calibrating the hardening parameters of the material model. As a result, the equivalent stress-strain curve of the material up to fracture is obtained.

Keywords: tensile tests; plastic anisotropy; strain localization; finite element method; crystal plasticity;

[*] Corresponding author: Mikhail Khadyko (mikhail.khadyko@ntnu.no)

1. Introduction

One of the basic and most important experimental tests in material science is the uniaxial tension test. A great variety of ways to perform the test on a given material exists, with different sizes and shapes of the specimens and different methods to apply the tensile load and measure the resulting displacements and forces. All these variations have a common core, defined by the way the material (or in our case an aluminium alloy) deforms plastically. At small strains, in the elastic and early plastic regime of deformation, the deformation of the specimen may be safely considered homogeneous throughout the cross-section. Consequently the stress may be considered homogeneous and is easily calculated as the ratio of the total force and cross-section area (either initial or current). In this regime of deformation the specimen may also be assumed, without much loss of accuracy, to deform homogeneously along its length, at least on some considerable length span in the centre. It allows for a convenient way to measure and calculate strains with strain gauges, extensometers, digital image correlation or other techniques. The problems arise when the strains reach some critical value and the specimen goes into another regime of deformation — diffuse necking [1]. The critical strain for necking is much lower than the ultimate strain at fracture for most important aluminium alloys. In the diffuse necking regime the deformation concentrates in some area of the specimen and the strain becomes highly heterogeneous. Moreover, the stress situation in the necking area becomes much more complex. In the homogeneous regime the component of the stress along the tensile axis is the only component of the stress tensor and is therefore equal to the equivalent stress, provided that the material is isotropic. If the material is anisotropic, the latter holds only in the reference direction. But in the necking area the heterogeneous deformation field produces a complex stress field with triaxiality deviating from one-third. It is still possible to find the average true stress component in the tensile direction as well as the average true strain in the necking area, but this true stress component will noticeably deviate from the equivalent stress [2]. The conceptual difficulty here is that we are seeking the properties of the material, but we measure the response of a specimen with all its constraints and instabilities. While the material continues to work-harden up until very large strains, we only have reliable information about its behaviour in a relatively small strain range, where the specimen is still geometrically stable.

The first attempt to overcome this problem was made by Bridgman [3]. His approach was analytical and consisted of finding the stress field in the neck region of a tensile specimen with circular cross-section and isotropic plastic behaviour of the material. The result was a

parameter which transformed the true stress in the neck of the specimen (smallest cross section) into the equivalent stress. Later other researchers tried to improve the initial solution aiming for better accuracy [4] or other specimen geometries [5], but after all the Bridgman correction for the true stress remains the most popular analytical method.

The main shortcomings of this solution are the much idealized assumed properties of the material and the specimen. The material must be isotropic, which makes the application of this method to highly anisotropic textured aluminium alloys very dubious. The correction in its initial form depends on the curvature of the neck region which is hard to measure, and the existing phenomenological methods, which avoid this measurement, sacrifice some accuracy [6]. So a way of extracting the equivalent stress as a function of strain from the tensile test after the onset of necking remains an important problem.

We propose a method of extracting this information from a specimen of arbitrary axisymmetric geometry and made of a material with arbitrary plastic anisotropy. Instead of an analytical solution we use a numerical solution based on the finite element method (FEM). Already in the 1970s, FEM was used to find stress-strain fields in the necking area [7, 8]. It has since then been used successfully to model localization up until fracture in uniaxial tension [9] and plane strain [10] and for anisotropic textured aluminium alloys [11]. Other examples of recent works, where FEM solutions of localization problems are validated by experimental data, include [12, 13].

The plastic anisotropy of the tested material is described by an anisotropic yield function. This kind of yield functions is also well established. Since the early work of Hill [14], different formulations have been proposed [15, 16]. This sort of functions was found to be an adequate representation of the plastic anisotropy of aluminium alloys, when fitted to experimental data [17]. A class of non-quadratic yield functions based on linear transformations of the stress deviator was proposed in [18] and discussed more generally in [19]. These yield functions typically use a large number of parameters to describe the shape of the yield surface of the material with high flexibility and accuracy. The drawback is the correspondingly high number of material tests necessary to identify these parameters.

To reduce the required number of tests in the parameter identification procedure, the tests were complemented by numerical simulations utilizing the crystal plasticity theory. Knowledge of the crystallographic texture and the plastic behaviour of the slip systems in the individual crystals of the material allow us to substitute some of the tests with simulations.

This method was first used in [20] and [21]. By now it is used by many researchers with relative success, especially in predicting the plastic strain anisotropy of metals and alloys [22]. Though crystal plasticity simulations may ignore some important physical mechanisms playing a role in the plastic response, they are in general cheaper than physical testing. The limits of this method are discussed in [23]. Crystal plasticity is used to find the yield surface of textured alloys in [24, 25, 26].

The method we propose is based on these techniques, well established theoretically and validated by experiments. We use 3D FEM simulations of a tensile specimen, with an anisotropic yield surface, found from crystal plasticity simulations. The true stress-strain response of the simulated specimen is then fitted to the response of the real specimen by optimizing the properties of the simulated material — its yield strength and hardening parameters. When these characteristics are found we can directly obtain the equivalent stress-strain response of the material.

In recent years several researchers have approached the problem using a similar framework. Zhano and Li [27] used an optimization procedure to extrapolate the stress after necking. Cabezas and Celentano [28] used FEM to find correction factors for cylindrical and plane steel specimens. Bogusz et al. [29] used digital image correlation and FEM simulations to compare correction factors from different analytical models. Ling [30] extrapolated the hardening from before necking and validated it with an FEM simulation of the post-necking deformation. Westermann et al. [31] used the same laser gauge measurement and a similar numerical simulation method as in this work, but for isotropic aluminium alloys. However, to the authors' best knowledge, the proposed combination of crystal plasticity, anisotropic material model and optimization technique to obtain the equivalent stress-strain curve all the way to failure for a ductile aluminium alloy has not been used before.

2. Experiments

2.1. Materials

Three aluminium alloys were used in the tests: 6060, 6082.50 and 6082.25. The chemical composition of the alloys is given in Table 1. The specimens were obtained from 10 mm thick and 90 mm wide extruded flat profiles at 90° to the extrusion direction and heat treated to five different tempers: T4, T6x, T6, T7 and O. The various heat treatments are described in Table 2. The alloys were analysed in the scanning electron microscope using electron back-

scattering diffraction (EBSD) and EDAX TSL OIM software to provide grain morphology and texture. The orientation distribution functions (ODF) for the three alloys are shown in Figure 1, Figure 2 and Figure 3. The EBSD measurements were carried out in the plane defined by the extrusion and normal directions of the profile, using 10 μm steps on a square grid for the 6060 alloy and 5 μm steps for the 6082 alloys. The ODFs were calculated from the pole figures in the EDAX TSL OIM software using a harmonic series expansion and triclinic sample symmetry [32]. The total number of measured orientations (or grains/subgrains) is 2611, 22416 and 25512 for 6060, 6082.50 and 6082.25 alloy, respectively. The grain structure of the alloys is presented in Figure 4. The textures and grain structures are typical for recrystallized alloys (6060) and non-recrystallized extruded alloys (6082), respectively. The 6060 alloy has an equi-axed, recrystallized grain structure, whereas the two 6082 alloys have a non-recrystallized structure with flat, pancake-shaped grains The most prominent texture component in all three alloys is a cube component, but the other orientations differ strongly between the 6060 alloy and the two 6082 alloys. The texture of the 6060 alloy is comprised of a strong cube texture with a minor Goss component, while the two 6082 alloys have a strong cube texture with orientations along the β-fibre, which runs from the Copper to the Brass orientation, through the S component.

2.2. Mechanical testing

Tensile tests were performed at room temperature on three specimens for each temper of each alloy, giving a total of 45 tests. The geometry of the specimen is shown in Figure 5. The cross-head velocity of the universal tensile testing machine was $1.2 \ \mathrm{mm/min}$, which corresponds to an initial strain rate of $5 \cdot 10^{-4} \mathrm{s^{-1}}$. The force and minimum diameter of the cross section in two normal directions were measured during the whole test until fracture. The measurements of the minimum diameter were performed with an in-house measuring rig. It consists of two lasers mounted normally to each other and to the tensile axis of the specimen. The lasers were projecting light beams with dimensions $13 \times 0.1 \ \mathrm{mm^2}$ across the specimen and on the detectors on the opposite side of the rig. The system used a high-speed, contact-less AEROEL XLS13XY laser gauge with 1 μm resolution, which was installed on a mobile frame. The sample was scanned at a frequency of 1200 Hz during the test and the measured data were transferred by the built-in electronics to the remote computer via fast Ethernet. This setup ensured that the minimum diameters of the specimen in two normal directions are accurately measured throughout the whole test.

We introduce a Cartesian coordinate system x, y, z, where x is the extrusion direction, y is the transverse direction in the flat profile and z is the normal direction (i.e. in the thickness direction of the profile). The tensile direction is then always in the y direction. If we denote the measured diameters D_x and D_z, and assume that the deformed cross section is elliptical in shape (which is a reasonable assumption for orthotropic material), then we may find the current cross-section area as

$$A = \frac{\pi}{4} D_x D_z \qquad (1)$$

The true (Cauchy) stress is found as

$$\sigma_y = \frac{F}{A} \qquad (2)$$

where F is the measured tensile force. If we also assume plastic incompressibility, the true logarithmic strain may be expressed as

$$\varepsilon_y = \ln\left(\frac{A_0}{A}\right) \qquad (3)$$

where A_0 is the initial cross-section area of the specimen. These measures only express the average response of the specimen after necking starts. Similarly when equivalent strains are discussed, logarithmic strain is used. It should be noted that the plastic incompressibility assumption may not hold at strains near fracture because of void nucleation and growth.

The strain ratio, denoted r_y, is here defined as

$$r_y = \frac{d\varepsilon_x}{d\varepsilon_z} \qquad (4)$$

where

$$d\varepsilon_x = \frac{dD_x}{D_x}, \quad d\varepsilon_z = \frac{dD_z}{D_z} \qquad (5)$$

Therefore, if we plot the logarithmic strain in the extrusion direction $\varepsilon_x = \ln(D_x / D_0)$ as a function of the logarithmic strain in the normal direction $\varepsilon_z = \ln(D_z / D_0)$, then r_y is the

slope of the resulting curve. The ratio r_y equals unity for isotropic materials, while values different from unity indicates anisotropic plastic flow. If the texture evolves significantly with plastic deformation, r_y is also expected to change.

3. Material modelling

3.1. Crystal plasticity

To establish a yield surface to use in the phenomenological yield function, the crystal plasticity theory is utilized. It is implemented numerically in a rate-dependent form with the Kalidindi hardening model [33, 34] and a Taylor-type polycrystal homogenisation [35].

3.1.1. Single crystal kinematics and kinetics

A finite deformation formulation is used. The total deformation gradient is multiplicatively decomposed into elastic and plastic parts [36]

$$F = F^e F^p \tag{6}$$

The plastic part F^p transforms the body from the initial configuration Ω_0 into the intermediate plastically deformed configuration $\bar{\Omega}$, see Figure 6. The elastic component F^e transforms the body from intermediate into the current configuration Ω with elastic deformation and rigid body rotation. The first transformation is due to slip on the slip systems, which are here represented by couples of vectors connected to the lattice. The lattice remains undeformed during this transformation. During the second transformation the lattice deforms and rotates together with the material. The intermediate configuration is thus unaffected by rigid body rotations, so the constitutive relations formulated in this configuration are objective. The following relations are based on [33]. The vectors m_0^α and n_0^α are the slip direction and slip plane normal vectors, respectively, for a slip system α in the initial and intermediate configuration, whereas m^α and n^α are the slip system vectors in the current configuration, rotated and stretched by the elastic deformation gradient F^e. These vectors are normal to each other in any configuration by definition. The plastic velocity gradient $\bar{L}^p$ in the intermediate configuration then has these vectors as a basis

$$\bar{L}^p = \dot{F}^p \left(F^p \right)^{-1} = \sum_{\alpha=1}^{n} \dot{\gamma}^\alpha m_0^\alpha \otimes n_0^\alpha \tag{7}$$

where $\dot{\gamma}^\alpha$ is the slip rate on slip system α in the intermediate configuration and n is the total number of slip systems. The elastic Green strain tensor $\bar{E}^e$ in the intermediate configuration may be defined as

$$\bar{E}^e = \frac{1}{2}\left[\left(F^e\right)^T F^e - I\right] = \frac{1}{2}\left(\bar{C}^e - I\right), \quad \bar{C}^e = \left(F^e\right)^T F^e \tag{8}$$

where $\bar{C}^e$ is the elastic right Cauchy-Green deformation tensor and I is the unity tensor. The second Piola-Kirchhoff stress tensor $\bar{S}$ in the intermediate configuration is obtained by pulling back the Cauchy stress tensor σ into this configuration

$$\bar{S} = \left(F^e\right)^{-1}\sigma \det F \left(F^e\right)^{-T} \tag{9}$$

This stress is power conjugate to the elastic Green strain and is found from the hyperelastic law

$$\bar{S} = \mathbf{C}_e^{\bar{S}} : \bar{E}^e \tag{10}$$

where $\mathbf{C}_e^{\bar{S}}$ is the fourth order tensor of elastic moduli. It has 3 independent components and hence describes the crystal anisotropy. The total power per unit volume $\dot{w}$ produced by the crystal consists of elastic (stored) and plastic (dissipated) parts

$$\dot{w} = \dot{w}^e + \dot{w}^p = \bar{S} : \dot{\bar{E}}^e + \bar{C}^e\bar{S} : \bar{L}^p \tag{11}$$

The plastic part of the total power may be also expressed through the power spent on every slip system if the resolved shear stress τ^α is introduced

$$\dot{w}^p = \sum_{\alpha=1}^{n} \tau^\alpha \dot{\gamma}^\alpha \tag{12}$$

where τ^α is connected to the second Piola-Kirchhoff stress through the slip system vector basis

$$\tau^\alpha = \bar{C}^e\bar{S} : \left(m_0{}^\alpha \otimes n_0{}^\alpha\right) \tag{13}$$

3.1.2. Flow and hardening rules

The plastic flow is described by a widely used rate-dependent rule proposed in [37] as

$$\dot{\gamma}^{\alpha} = \dot{\gamma}_0 \left(\frac{\left| \tau^{\alpha} \right|}{\tau_c^{\alpha}} \right)^{\frac{1}{m}} \mathrm{sgn}\left(\tau^{\alpha} \right) \tag{14}$$

where $\dot{\gamma}_0$ is the reference slip rate, m is the instantaneous strain rate sensitivity and τ_c^{α} is the history dependent yield strength of slip system α. The hardening rate of each slip system is defined by

$$\dot{\tau}_c^{\alpha} = \sum_{\beta=1}^{n} h^{\alpha\beta} \left| \dot{\gamma}^{\beta} \right| \tag{15}$$

where $h^{\alpha\beta}$ are the slip hardening rates developing on slip system α because of slip on system β. They may be decomposed into

$$h^{\alpha\beta} = q^{\alpha\beta} h^{\beta} \tag{16}$$

where $q^{\alpha\beta}$ is a matrix of self-hardening and latent-hardening coefficients and h^{β} may be defined as proposed in [34]

$$h^{\beta} = h_0 \left(1 - \frac{\tau_c^{\beta}}{\tau_s} \right)^{a} \tag{17}$$

Here h_0 is the initial hardening rate, τ_s is the resolved shear stress saturation value and a is the power law parameter. The initial slip resistance τ_{c0}^{α} is assumed equal for all slip systems.

3.1.3. Polycrystal modelling

The material sample includes too many orientations to be represented numerically as it is, so we represent it with a reduced number of orientations, chosen by analysing its texture. It has been shown that this reduced number is enough to accurately represent the properties of the material in numerical simulations [26]. Each grain is represented by its orientation and volume fraction. We assume the volume fraction to be equal for all grains.

The Taylor model [35] assumes that all grains undergo the same strain as the whole specimen. Stress equilibrium between the grains is then not satisfied. The stress in the specimen is found as an average, i.e.

$$\boldsymbol{\sigma} = \frac{1}{n} \sum_{i=1}^{n} \boldsymbol{\sigma}_g^i \tag{18}$$

where $\boldsymbol{\sigma}_g^i$ is the Cauchy stress in grain i and n is the total number of grains. The use of the Taylor model (here the so-called full-constraint variant is used) against a FEM model of a polycrystal and various relaxed constraint models is discussed in [23] and [38]. The conclusion is that no method is universally good at describing the polycrystal response, while the Taylor model has the advantage of simplicity and computational efficiency.

Some common assumptions are made about the material. The initial value of the slip resistance is the same on all slip systems, as well as the other material parameters; i.e., the material has no history of prior deformation. The influence of precipitates, inclusions, dispersoids or any other factors is ignored; just pure Schmid slip is considered, so that crystallographic texture is the only source of plastic anisotropy. This assumption may seem crude, but including these other factors is a very difficult task and for most cases texture is by far the main source of anisotropy [39].

3.2. Continuum plasticity

The behaviour of the material in the tensile tests is modelled by an anisotropic hypoelastic-plastic continuum model. The main features of this model are: small elastic and finite plastic strains, isotropic elasticity and orthotropic yield surface, associated plastic flow, isotropic strain hardening and corotational formulation. The corotational formulation is used to simplify the plastic anisotropy formulation. The principal directions of the plastic orthotropy are aligned with the coordinate system, connected to the unrotated configuration. The axes of this system are assumed to remain orthogonal during deformation. The corotational Cauchy stress is also defined in this system.

The corotational stress and rate-of-deformation tensors are defined [40] as

$$\hat{\boldsymbol{\sigma}} = \boldsymbol{R}^T \boldsymbol{\sigma} \boldsymbol{R} \tag{19}$$

$$\hat{\boldsymbol{D}} = \boldsymbol{R}^T \boldsymbol{D} \boldsymbol{R} \tag{20}$$

where $\boldsymbol{D}$ is the rate-of-deformation tensor in the current configuration, $\boldsymbol{\sigma}$ is the Cauchy stress tensor and $\boldsymbol{R}$ is the rotation tensor found from the polar decomposition of the deformation gradient tensor

$$F = RU \tag{21}$$

The corotational rate-of-deformation tensor is decomposed into a sum of elastic and plastic parts

$$\hat{D} = \hat{D}^e + \hat{D}^p \tag{22}$$

In the hypoelastic formulation the corotational stress rate is connected to the corotational deformation rate

$$\dot{\hat{\sigma}} = \hat{C}_{el}^{\sigma} : \hat{D}^e \tag{23}$$

where $\hat{C}_{el}^{\sigma}$ is the fourth order tensor of elastic moduli. Elastic isotropy is assumed for the material, so only two independent parameters are enough to define this tensor, i.e. the Young's modulus E and the Poisson ratio ν.

The yield function is formulated as

$$f(\hat{\sigma}, \bar{\varepsilon}) = \bar{\sigma}(\hat{\sigma}) - \kappa(\bar{\varepsilon}) \tag{24}$$

where $\bar{\varepsilon}$ is the equivalent plastic strain, $\bar{\sigma}$ is the equivalent stress and κ is the flow stress in uniaxial tension in the reference direction. The evolution of the flow stress κ is described by a two-term Voce rule [41]

$$\kappa(\bar{\varepsilon}) = \kappa_0 + \sum_{i=1}^{2} Q_i \left(1 - \exp\left(-\frac{\theta_i}{Q_i} \bar{\varepsilon} \right) \right) \tag{25}$$

where κ_0 is the yield stress, and Q_i and θ_i are model parameters governing the work-hardening.

The corotational plastic rate-of-deformation tensor evolves according to the associated flow rule

$$\hat{D}^p = \dot{\lambda} \frac{\partial f}{\partial \hat{\sigma}} \tag{26}$$

where $\dot{\lambda}$ is the plastic multiplier, which satisfies the loading-unloading conditions, written in Kuhn-Tucker form as

$$\dot{\lambda} \geq 0, \quad f \leq 0, \quad f\dot{\lambda} = 0 \tag{27}$$

The form of the equivalent stress used here, called Yld2004-18p by the authors, was developed in [19] to represent complex shapes of anisotropic yield surfaces, viz.

$$\bar{\sigma} = \left(\frac{1}{4}\phi\right)^{\frac{1}{m}} \tag{28}$$

where

$$\phi = \phi\left(\tilde{\mathbf{S}}', \tilde{\mathbf{S}}''\right) = \sum_{i=1}^{3}\sum_{j=1}^{3}\left|\tilde{S}'_i - \tilde{S}''_j\right|^m \tag{29}$$

In this equation m is the shape parameter while $\tilde{\mathbf{S}}'$ and $\tilde{\mathbf{S}}''$ represent the principal values of the stress tensors $\tilde{s}'$ and $\tilde{s}''$. These stress tensors are in turn produced by linear transformations of the corotational stress tensor

$$\tilde{s}' = \mathbf{C}' : \hat{s} = \mathbf{C}' : \mathbf{T} : \hat{\sigma} \tag{30}$$

$$\tilde{s}'' = \mathbf{C}'' : \hat{s} = \mathbf{C}'' : \mathbf{T} : \hat{\sigma} \tag{31}$$

where the fourth order tensor $\mathbf{T}$ transforms the corotational stress $\hat{\sigma}$ into its deviatoric part $\hat{s}$ and the fourth order tensors $\mathbf{C}'$ and $\mathbf{C}''$ contain the coefficients describing the anisotropy of the material. In the orthotropic case 9 independent coefficients are enough to define each of them, and in Voigt notation they read

$$\mathbf{C}' = \begin{bmatrix} 0 & -c'_{12} & -c'_{13} & 0 & 0 & 0 \\ -c'_{21} & 0 & -c'_{23} & 0 & 0 & 0 \\ -c'_{31} & -c'_{32} & 0 & 0 & 0 & 0 \\ 0 & 0 & 0 & c'_{44} & 0 & 0 \\ 0 & 0 & 0 & 0 & c'_{55} & 0 \\ 0 & 0 & 0 & 0 & 0 & c'_{66} \end{bmatrix} \tag{32}$$

$$C'' = \begin{bmatrix} 0 & -c''_{12} & -c''_{13} & 0 & 0 & 0 \\ -c''_{21} & 0 & -c''_{23} & 0 & 0 & 0 \\ -c''_{31} & -c''_{32} & 0 & 0 & 0 & 0 \\ 0 & 0 & 0 & c''_{44} & 0 & 0 \\ 0 & 0 & 0 & 0 & c''_{55} & 0 \\ 0 & 0 & 0 & 0 & 0 & c''_{66} \end{bmatrix} \tag{33}$$

If all the anisotropy coefficients c'_{ij} and c''_{ij} are set to unity, this yield function will reduce to an isotropic high-exponent yield function. The total number of model parameters of the continuum plasticity model to identify is 26: two elasticity coefficients, E and v; the initial yield stress, κ_0; four hardening parameters, Q_i and θ_i, $i = 1, 2$; the shape parameter, m; and the 18 anisotropy coefficients, c'_{ij} and c''_{ij}.

4. Parameter identification

4.1. Slip system level

The initial step of the method is to obtain an estimate of the yield surface shape from the crystal plasticity (CP) simulations. The microstructural study provided information about the orientations of the grains in the alloys and allowed to build the corresponding ODF. To run the CP model this information needed to be transformed into a convenient set of orientations which accurately represent the texture. Different methods of doing this exist, e.g. [42], [43]. The one used in this work is the following. A total of 1000 grain orientations were taken randomly from the whole set of measured orientations. The number is small enough to provide reasonable computation times and big enough to represent the influence of all texture components on the shape of the yield surface [44]. The representativeness of this random set in relation to the components of the real texture was checked by making several random choices of 1000 orientations, calculating the ODFs of those reduced sets and comparing them with the ODF of the real texture. The differences were insubstantial, so this method was used for all three alloys.

The initial shape of the yield surface, i.e. the initial plastic anisotropy, is commonly believed to depend mostly on the texture, and in the utilized CP model it depends solely on the texture. Hardening is assumed isotropic in the continuum model, meaning that this shape stays the same throughout the deformation. The factor that defines the shape of the yield surface of the polycrystal is which slip systems in the constituent crystals activate and which

do not. Thus, the shape of the yield surface calculated for alloys with different hardening parameters should be the same — as for example in [45] and [46] the calculated yield surfaces for two different 6063 alloy specimens are the same. In addition the yield surfaces were calculated with the same texture, but different sets of hardening parameters with the numerical set up used in this work. The results were also identical.

In our case we deal with three yield surfaces, corresponding to three different textures. The same yield surface is used for all tempers of the same alloy. The hardening parameters we use are given in Table 3.

It should be mentioned that there may be some factors influencing the crystallographic slip, which may lead to anisotropic hardening or a totally different yield surface than the one found on the basis of our assumptions. Some of them played their role in the response of the 6082.50 alloy, but accounting for them is a difficult task and outside the scope of this article.

The crystal plasticity model is implemented into a user material subroutine for LS-DYNA. The subroutine utilizes an explicit integration scheme by Grujicic and Batchu [47]. Explicit time integration of the momentum equations is used. The material is represented by a single eight-node element with one Gauss point (reduced integration). Using more elements in the Taylor model increases the computation time significantly, without substantial improvement of accuracy. The yield surface is calculated as follows. The element is subjected to a range of tensile and shear strain combinations, creating a cloud of points in the strain space. The straining stops each time the specific plastic work of deformation reaches a value of 0.5 MPa approximately corresponding to incipient yielding. The resulting stress responses are also represented by points in stress space, lying on the yield surface, which corresponds to this value of plastic work. Then an optimization script uses these stress points and the anisotropic yield criterion defined by Eq. (24) to find the components of the transformation tensors in Eqns. (32) and (33), see Table 4 for the obtained values. The resulting yield surfaces are shown in Figure 7, where σ_x is the normal stress in the reference direction, which is here the extrusion direction, σ_y is the normal stress in the transverse direction of the flat profile, and $\sigma_0 \equiv \kappa_0$ is the initial yield stress in the reference direction. The contours represent lines of constant shear stresses σ_{xy} in the plane of the flat profile. The calculated yield surfaces fit well with the ones found for alloys with similar texture/microstructure in [45].

4.2. Continuum level

The next step is the application of these results to the continuum plasticity model and fitting of this model to the experimental data. The mesh of the FE model of the tensile specimen is shown in Figure 8. Owing to the orthotropic symmetry and to reduce computation time only $1/8^{th}$ of the specimen is modelled. The dimensions of the smallest elements used in the necking area are $0.3 \times 0.3 \times 0.07$ mm^3. Several test simulations with larger and smaller elements were run to ensure that at this element size the mesh does not affect the solution. Symmetrical boundary conditions are utilized and constant velocity is applied to the upper plane, where the specimen is fixed to the test machine. It should be noted that in the experiments necking occurs at a point determined by the imperfections of the specimen, while in the simulation the mesh is made without imperfections and the specimens necks in the centre (at the corresponding edge of the mesh). The eight-node constant stress solid element with reduced integration available in LS-DYNA was used in the simulations. Explicit time integration was chosen, since some initial test runs showed that implicit integration for this model does not provide any considerable advantage in speed, stability or accuracy. Mass scaling (by increasing the density of the material) was used to reduce the simulation time. It was then checked that the kinetic energy was still very small compared with the total energy of the specimen, to ensure quasi-static loading conditions.

The elastic-plastic behaviour of the material is modelled as described in Section 3.2. The 18 coefficients of the two linear transformations of the stress tensor used to describe the plastic anisotropy were determined as described in Section 4.1. The elastic constants were set to nominal values for aluminium alloys. It thus remains to determine the parameters κ_0, Q_i and θ_i of the two-term Voce hardening rule. This is done using LS-OPT [48] – an optimization tool that interacts with LS-DYNA. Within each iteration LS-OPT runs simulations with LS-DYNA varying these parameters within prescribed intervals. A true stress-strain curve for the central cross-section area (where necking occurs) is calculated at the end of each simulation. These curves are compared to the true stress-strain curves found from the experiments for the corresponding alloy. LS-OPT compares the experimental curve with the simulated one, calculates the mean squared error and varies the hardening rule parameters in such a way that in the next iteration the mean squared error is reduced. After usually 15-20 iterations the mean squared error reduces from the range of 1-100 to around $1 \cdot 10^{-5}$ and more iterations do not further reduce it.

5. Results

5.1. Continuum plasticity model calibration

The results of the optimization procedure described in the previous section are presented in Figure 9 to Figure 11 for the three alloys in terms of the true stress-strain curves for the five tempers. The true stress-strain curves, obtained for three specimens of each alloy-temper combination, are in good agreement with each other, so only one typical curve is shown. In general, the two-term Voce hardening rule led to very good fit with small error for most of the simulations. The largest error is observed for 6060-T7, where the overall shape of the curve could not be accurately reproduced. A better fit for this case would have been obtained by using a three-term Voce hardening rule. One may notice that the simulated curves for the 6060 alloy tend to bend upwards at the end of the simulation, as if the work-hardening rate suddenly increases. This is a numerical artefact, caused by the very large deformation of the elements in the necking zone. This unphysical behaviour is not observed for the 6082 alloys, because of their lower ductility.

The simulation model accounts for plastic anisotropy, and the correspondence of the anisotropy in plastic flow in the simulations and experiments was also checked. This is done by comparing the strain ratio r_y obtained in experiments and simulations. The results are shown in Figure 12 to Figure 14. The experimental and simulated value of r_y are reasonably close for alloys 6060 and 6082.25, while the discrepancy is large for 6082.50. Also noticeable is the low ductility of this alloy compared to the very similar 6082.25 alloy and the instabilities seen in the measured values of r_y for the T6, T6x and T7 tempers. The error in the predicted value of r_y means that the yield surface predicted solely on the basis of texture is inaccurate, at least for the actual stress state. While slip on crystallographic slip systems is the mode of deformation of both these alloys, the slip systems activated are very different. Thus, the assumption of equal initial slip resistance and hardening parameters on all slip systems is not adequate for this alloy.

The main difference between these two 6082 alloys is the contents of Cr (and to some extent Cu) and the presence of Cr dispersoids (see Table 1). It is reasonable to assume that the influence of these elements on the slip is very strong and cannot be ignored in the modelling of the material. Another point of interest is that in the case of the 6060 alloy we observe significant change in the r_y value throughout the test. The most obvious reason for this is an

evolution of the texture with the deformation. This means that the shape of the yield surface also evolves and our assumption of isotropic hardening is reasonable, but not generally correct. The 6082 alloys demonstrate much less evolution of r_y, so at least for these alloys, the assumption of isotropic hardening holds with reasonable accuracy.

A comparison between the necking zones of the specimens at fracture as observed in the experiments and predicted by the finite element model is presented for two different alloys and tempers in Figure 15. In the figure, the experimental and numerical results have been superimposed. Considering the discrepancy in the r_y ratio between the model and the experiment, the curvature of the neck zone is well reproduced in both cases.

5.2. Equivalent strain-stress

The main result of the model calibration is the parameters in the Voce hardening rule defining the equivalent stress-strain curves of the materials. The results are compiled in Figure 16 to Figure 18. The equivalent stress-strain curves are plotted until fracture. For most alloys/tempers the equivalent stress-strain curves obtained for the three specimens tested are in very good agreement with each other. Therefore only the averaged equivalent stress-strain curve is shown in the figures. In Table 5 the numerical values of the hardening parameters for typical specimens are presented.

The first notable result is the profound effect of the heat treatment on the initial strength and work-hardening of the three alloys. A detailed discussion of the physical mechanisms responsible for the observed behaviour will be presented elsewhere. The second observation is the large difference in ductility between the alloys. For the 6060 alloy even the usually less ductile T6 and T7 tempers fracture at more than 120% strain. The difference in ductility between 6082.50 and 6082.25 is all the more surprising, considering their very similar chemical composition.

The "apparent hardening rate" at large strains is much higher for the true stress-strain curves than for the equivalent stress-strain curves, see Figure 19 for two examples. The reason for this is obviously the contribution of the triaxial stress field to the true stress measured after necking. The hydrostatic stress does not contribute to the equivalent stress, which is based on linear transformations of the stress deviator. Figure 19 shows another difference: the equivalent stress may be either higher or lower than the true stress even before necking for the different alloys. The reason for this is that the specimens are oriented at 90° to the extrusion

direction, which was taken here as the reference direction, and the stress in any direction other than the extrusion direction depends on the anisotropy of the yield surface. In this case, the 90° flow stress is either lower (6060) or higher (6082.25) than the 0° flow stress.

The method of using an anisotropic plasticity model to find the equivalent stress was compared to a similar method, but using an isotropic plasticity model (adopting the von Mises yield criterion) and the modified Bridgman correction method as it is formulated in [6]. The comparison of obtained stress-strain curves is shown in Figure 20. The results are noticeably different. The Bridgman correction overestimates the hardening rate, while the isotropic plasticity model underestimates the equivalent stress. However, compared with the true stress-strain curve the three equivalent stress-strain curves are in reasonable agreement.

6. Discussion and conclusions

While it is hard to evaluate how accurately we predicted the equivalent stress-strain curves, it is possible to re-evaluate the accuracy of the initial assumptions in light of the results.

The first issue is the yield function. The full-constraint Taylor simulations predicted the yield function rather well for two of the three alloys, as judged based on the measured strain ratio r_y. In the case of the 6082.50 alloy it looks like some factors skewed the yield surface completely out of the texture-defined shape. Computational crystal plasticity has been developing for decades, but accurate predictions of yield surface shapes, which account for texture, grain morphology, precipitates, hard particles, dispersoids, dislocation substructures and other possible factors are far from full realization. Hence, further development of the computational crystal plasticity should improve the accuracy of our model. Other types of homogenization could be tested, like self-consistent models, relaxed constraint models or the crystal plasticity finite element method. The assumption of isotropic hardening seems to be fulfilled with good accuracy for the two 6082 alloys, but not for the 6060 alloy. The yield surface defines the direction of the plastic strain rate, and this direction was gradually changing according to e.g. Figure 12. In case of the 6060 alloy the initial value of the strain ratio r_y, and ergo the yield surface shape, was predicted quite well by the full-constraint Taylor model. So the evolution of the r_y ratio is most probably due to evolution of the texture. To improve the predictive power of our model, an evolving yield surface could be implemented in the continuum plasticity, with evolution based on the predictions by the

crystal plasticity theory. The first problem is a considerable increase in the computation time and the second is that the predictions of texture evolution by crystal plasticity are also still not very accurate. In any case, the difference between the equivalent stress-strain curves obtained with the isotropic and anisotropic versions of the continuum plasticity model is not large, see Figure 20, and the predicted hardening rate is approximately the same (compared to the Bridgman correction), meaning that improvements in this area would not be very cost-effective.

The second issue is the two-term Voce hardening rule. It is rather flexible and fits to most of the 6xxx alloys hardening curves well, but in some cases, like 6082.50-T4 or especially 6060-T7, it was likely not flexible enough to reproduce some of the features of the true stress-strain curve. More terms in the Voce hardening rule or another hardening rule altogether could be used, though more complex hardening rules again means increasing the computation time.

Some improvements could be done in FEM implementation of the methods too. An accurate description of the necking zone requires a dense mesh. In addition very high local strains distort the elements immensely. To prevent the elements from too much of shape distortion and associated problems, they are initially not cubic but flatted. However, the model still shows some artificial stiffening at the latest stages of deformation, around 140-150% logarithmic strain. This could be prevented by re-meshing the geometry at least partly after a certain strain is reached. The main problem with all kinds of measures that makes the model more accurate, but more complicated, is that it is run not once but sometimes hundreds of times by LS-OPT to optimize the hardening parameters, meaning that any increase in computation time for one simulation leads to a much larger increase in the total optimization time.

The equivalent stress-strain curves were found for deformation after necking and large strain values until fracture. It should be remembered though that what was really found is the equivalent stress-strain curves in an isotropically hardened two-term Voce material with Yld2004-18p yield criterion implemented in an FEM mesh. How well the predicted equivalent stress-strain curves correspond to the real curves depends on how accurate the assumptions and the models are. For practical applications the accuracy of the results is determined by how well it predicts the forces and displacements in various problems, so at least for the problem of necking in a cylindrical rod it is very accurate. In any case, until a

method of measuring stress *in situ* is developed, any stress estimate after necking will be just an estimate, depending on abstractions and assumptions. The comparison in Figure 20 indicates that this model is the next step towards a more accurate estimate of the equivalent stress-strain curves at large strains.

Acknowledgements

References

[1] Considère M. Memoire sur l'emploi du fer et de l'acier dans les constructions. Dunod, 1885.

[2] Mirone G. Role of stress triaxiality in elastoplastic characterization and ductile failure prediction. Eng Fract Mech 2007;74:1203-1221.

[3] Bridgman P. The stress distribution at the neck of a tension specimen. T Am Soc Met 1944;32:553-574.

[4] Davidenkov N, Spiridonova N. Analysis of the state of stress in the neck of a tension test specimen, Proceedings of American Society of Testing Materials, 1946;46:1147-1158.

[5] Aronofsky J. Evaluation of Stress Distribution in the Symmetrical Neck of Flat Tensile Bars. J Appl Mech 1951;75-84.

[6] Le Roy G, Embury J, Edwards G, Ashby M. A model of ductile fracture based on the nucleation and growth of voids. Acta Metall Mater 1981;29:1509-1522.

[7] Needleman A. A numerical study of necking in circular cylindrical bar. J Mech Phys Solids 1972;20:111-127.

[8] Norris Jr D, Moran B, Scudder J, Quinones D. A computer simulation of the tension test. J Mech Phys Solids 1978;26:1-19.

[9] Tvergaard V, Needleman A. Analysis of the cup-cone fracture in a round tensile bar. Acta Metall Mater 1984;32:157-169.

[10] Tvergaard V, Needleman A, Lo KK. Flow localization in the plane strain tensile test. J Mech Phys Solids 1981;29:115-142.

[11] Fourmeau M, Børvik T, Benallal A, Lademo O, Hopperstad O. On the plastic anisotropy of an aluminium alloy and its influence on constrained multiaxial flow. Int J Plasticity 2011;27:2005-2025.

[12] Dunand M, Mohr D. On the predictive capabilities of the shear modified Gurson and the modified Mohr–Coulomb fracture models over a wide range of stress triaxialities and Lode angles. J Mech Phys Solids 2011;59:1374-1394.

[13] Nam AW, Choung J. Prediction of failure strain according to stress triaxiality of a high strength marine structural steel. Collision and Grounding of Ships and Offshore Structures 2013;69.

[14] Hill R. A theory of the yielding and plastic flow of anisotropic metals. P Roy Soc Lond A Mat 1948;193:281-297.

[15] Hosford W. A generalized isotropic yield criterion. J Appl Mech 1972;39:607.

[16] Bron F, Besson J. A yield function for anisotropic materials application to aluminum alloys. Int J Plasticity 2004;20:937-963.

[17] Barlat F, Maeda Y, Chung K, Yanagawa M, Brem J, Hayashida Y, Lege D, Matsui K, Murtha S, Hattori S. Yield function development for aluminum alloy sheets. J Mech Phys Solids 1997;45:1727-1763.

[18] Aretz H, Barlat F. General orthotropic yield functions based on linear stress deviator transformations, AIP Conference Proceedings, 2004;712:147.

[19] Barlat F, Aretz H, Yoon J, Karabin M, Brem J, Dick R. Linear transfomation-based anisotropic yield functions. Int J Plasticity 2005;21:1009-1039.

[20] Barlat F. Crystallographic texture, anisotropic yield surfaces and forming limits of sheet metals. Mat Sci Eng 1987;91:55-72.

[21] Barlat F, Richmond O. Prediction of tricomponent plane stress yield surfaces and associated flow and failure behavior of strongly textured FCC polycrystalline sheets. Mat Sci Eng 1987;95:15-29.

[22] Choi S-H, Brem J, Barlat F, Oh K. Macroscopic anisotropy in AA5019A sheets. Acta Mater 2000;48:1853-1863.

[23] Grytten F, Holmedal B, Hopperstad OS, Børvik T. Evaluation of identification methods for YLD2004-18p. Int J Plasticity 2008;24:2248-2277.

[24] Beradai C, Berveiller M, Lipinski P. Plasticity of metallic polycrystals under complex loading paths. Int J Plasticity 1987;3:143-162.

[25] Zattarin P, Lipinski P, Rosochowski A. Numerical study of the influence of microstructure on subsequent yield surfaces of polycrystalline materials. Int J Mech Sci 2004;46:1377-1398.

[26] Saai A, Dumoulin S, Hopperstad O. Influence of Texture and Grain Shape on the Yield Surface in Aluminium Sheet Material Subjected to Large Deformations, AIP Conference Proceedings, 2011;1353:85.

[27] Zhano K, Li Z. Numerical analysis of the stress-strain curve and fracture initiation for ductile material. Eng Fract Mech 1994;49:235-241.

[28] Cabezas EE, Celentano DJ. Experimental and numerical analysis of the tensile test using sheet specimens. Finite Elem Anal Des 2004;40:555-575.

[29] Bogusz P, Popławski A, Morka A, Niezgoda T. Evaluation of true stress in engineering materials using optical deformation measurement methods. Journal of KONES Powertrain and Transport 2012;19.

[30] Ling Y. Uniaxial true stress-strain after necking. AMP J Tech 1996;5:37-48.

[31] Westermann I, Pedersen K, Furu T, Børvik T, Hopperstad OS. Effects of particles and solutes on the strength, work-hardening and ductile fracture of aluminium alloys. Submitted for possible journal publication 2013.

[32] Engler O, Randle V. Introduction to texture analysis: macrotexture, microtexture, and orientation mapping. CRC press, 2010.

[33] Needleman A, Asaro R, Lemonds J, Peirce D. Finite element analysis of crystalline solids. Comput Method Appl M 1985;52:689-708.

[34] Kalidindi SR, Bronkhorst CA, Anand L. Crystallographic texture evolution in bulk deformation processing of FCC metals. J Mech Phys Solids 1992;40:537-569.

[35] Taylor GI. The Mechanism of Plastic Deformation of Crystals. Part I. Theoretical. P Roy Soc Lond A Mat 1934;145:362-387.

[36] Lee E, Liu D. Finite-Strain Elastic—Plastic Theory with Application to Plane-Wave Analysis. J Appl Phys 1967;38:19-27.

[37] Hutchinson J. Bounds and self-consistent estimates for creep of polycrystalline materials. P Roy Soc Lond A Mat 1976;348:101-127.

[38] Li S, Engler O, Van Houtte P. Plastic anisotropy and texture evolution during tensile testing of extruded aluminium profiles. Model Simul Mater Sc 2005;13:783-795.

[39] Kocks UF, Tomé CN, Wenk H-R. Texture and anisotropy: preferred orientations in polycrystals and their effect on materials properties. Cambridge university press, 2000.

[40] Belytschko T, Liu WK, Moran B. Nonlinear finite elements for continua and structures. in: Chichester, New York, John Wiley, 2000.

[41] Voce E. The relationship between stress and strain for homogeneous deformation. J Inst Met 1948;74:537-562.

[42] Melchior MA, Delannay L. A texture discretization technique adapted to polycrystalline aggregates with non-uniform grain size. Comp Mater Sci 2006;37:557-564.

[43] Böhlke T, Haus U-U, Schulze V. Crystallographic texture approximation by quadratic programming. Acta Mater 2006;54:1359-1368.

[44] Lequeu P, Gilormini P, Montheillet F, Bacroix B, Jonas J. Yield surfaces for textured polycrystals—I. Crystallographic approach. Acta Metall Mater 1987;35:439-451.

[45] Achani D, Hopperstad OS, Lademo OG. Behaviour of extruded aluminium alloys under proportional and non-proportional strain paths. J Mater Process Tech 2009;209:4750-4764.

[46] Pedersen KO, Lademo OG, Berstad T, Furu T, Hopperstad OS. Influence of texture and grain structure on strain localisation and formability for AlMgSi alloys. J Mater Process Tech 2008;200:77-93.

[47] Grujicic M, Batchu S. Crystal plasticity analysis of earing in deep-drawn OFHC copper cups. J Mat Sci 2002;37:753-764.

[48] Stander N, Roux W, Goel T, Eggleston T, Craig K. LS-OPT user's manual. Livermore software technology corporation 2008.

Tables

Table 1: Chemical composition of the alloys in wt%.

Alloy	Fe	Si	Mg	Mn	Cr	Cu	Zn	Ti
6060	0.193	0.422	0.468	0.015	0.000	0.002	0.005	0.008
6082.50	0.200	1.020	0.670	0.540	0.001	0.003	0.005	0.010
6082.25	0.180	0.880	0.600	0.530	0.150	0.020	0.005	0.011

Table 2: Heat treatment of the specimens to different tempers.

Temper	Stage 1	Stage 2	Stage 3	Stage 4	Stage 5
T4	540°C in salt bath for 15 min	Fast water cooling	One week at room temperature	___	___
T6x	540°C in salt bath for 15 min	Fast water cooling	15 min at room temperature	185°C in oil bath for one hour	Air cooling
T6	540°C in salt bath for 15 min	Fast water cooling	15 min at room temperature	185°C in oil bath for five hours	Air cooling
T7	540°C in salt bath for 15 min	Fast water cooling	15 min at room temperature	185°C in oil bath for one week	Air cooling
O	540°C in salt bath for 15 min	Fast water cooling	15 min at room temperature	350°C in salt bath for twenty four hours	Air cooling

Table 3: Crystal plasticity model parameters used in the yield surface calculations.

c_{11}, MPa	c_{12}, MPa	c_{44}, MPa	$\dot{\gamma}_0$, s^{-1}	m	$q^{\alpha\beta}$, $\alpha \neq \beta$	h_0, MPa	a	τ_s, MPa	τ_{c0}^{α}, MPa
106430	60350	28210	0.010	0.005	1.40	411.25	1.354	104.02	46.70

Table 4: Coefficients of the YLD2004-18p yield function.

Coefficients	6060	6082.50	6082.25
c'_{12}	0.3050	0.8200	0.8178
c'_{13}	0.8051	1.3231	1.3225
c'_{21}	-0.3320	0.9911	0.9947
c'_{23}	0.5246	1.3224	1.3271
c'_{31}	-0.4386	0.2510	0.2568
c'_{32}	0.6322	0.5384	0.5350
c'_{44}	0.9768	1.2124	1.2029
c'_{55}	1.0000	1.0000	1.0000
c'_{66}	1.0000	1.0000	1.0000
c''_{12}	0.8578	-0.1219	-0.1288
c''_{13}	-0.2922	0.7228	0.7223
c''_{21}	1.0911	1.1599	1.1617
c''_{23}	0.8548	1.3144	1.3056
c''_{31}	1.1442	0.9191	0.9130
c''_{32}	0.6040	0.6100	0.6049
c''_{44}	-0.2170	0.8633	0.8661
c''_{55}	1.0000	1.0000	1.0000
c''_{66}	1.0000	1.0000	1.0000

Table 5: The obtained parameters for the two-term Voce hardening rule.

Alloy/temper	κ_0, MPa	Q_1, MPa	θ_1, MPa	Q_2, MPa	θ_2, MPa
6060-T4	64.00	72.64	1402.52	104.67	395.35
6060-T6	167.00	43.63	1652.83	57.70	85.00
6060-T6x	65.00	60.92	1646.22	102.96	255.07
6060-T7	125.00	27.36	2623.50	51.95	724.50
6060-O	35.00	46.36	1732.53	70.09	171.64
6082.50-T4	135.00	140.53	1661.71	148.90	252.71
6082.50-T6	250.00	65.20	51322.6	66.13	530.16
6082.50-T6x	250.00	38.65	48547.3	99.14	899.76
6082.50-T7	190.00	56.17	2528.25	30.52	110.22
6082.50-O	38.00	36.95	2129.88	94.77	465.48
6082.25-T4	157.00	143.03	1961.54	105.74	269.89
6082.25-T6	305.00	46.59	1344.37	54.13	107.42
6082.25-T6x	300.00	66.13	1296.66	59.76	104.59
6082.25-T7	170.00	44.35	1515.79	45.51	460.98
6082.25-O	65.00	45.88	2179.59	87.46	319.21

Figures
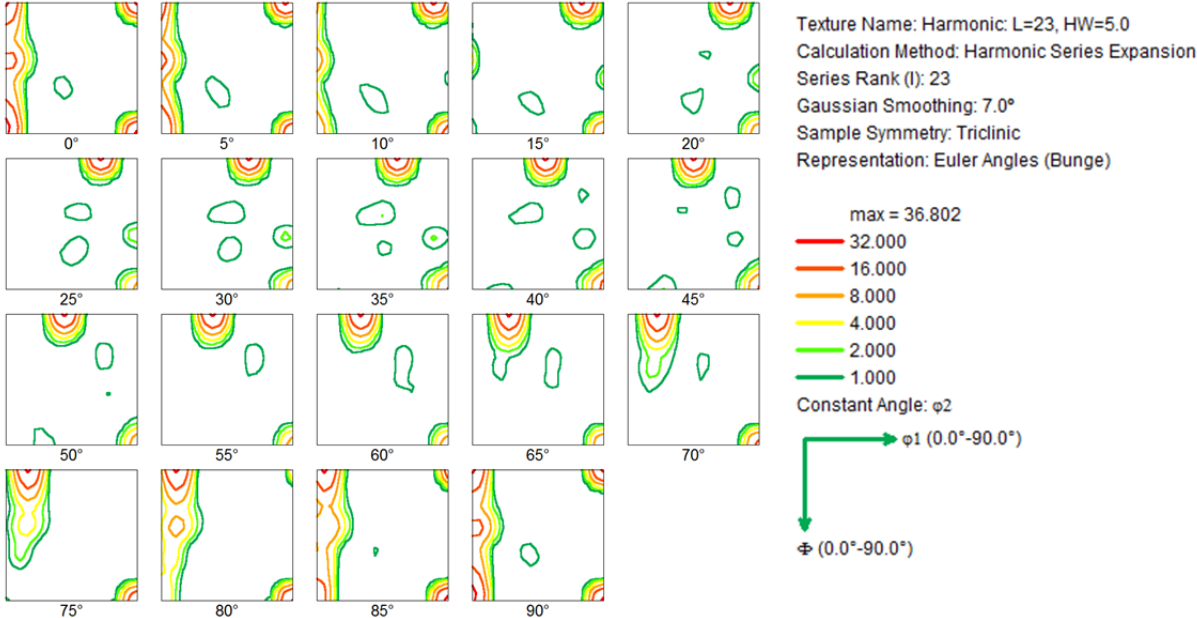
Figure 1: Orientation distribution function for the 6060 alloy.

Texture Name: Harmonic: L=23, HW=5.0
Calculation Method: Harmonic Series Expansion
Series Rank (I): 23
Gaussian Smoothing: 7.0°
Sample Symmetry: Triclinic
Representation: Euler Angles (Bunge)

max = 24.411
32.000
16.000
8.000
4.000
2.000
1.000
Constant Angle: φ2

φ1 (0.0°-90.0°)

Φ (0.0°-90.0°)
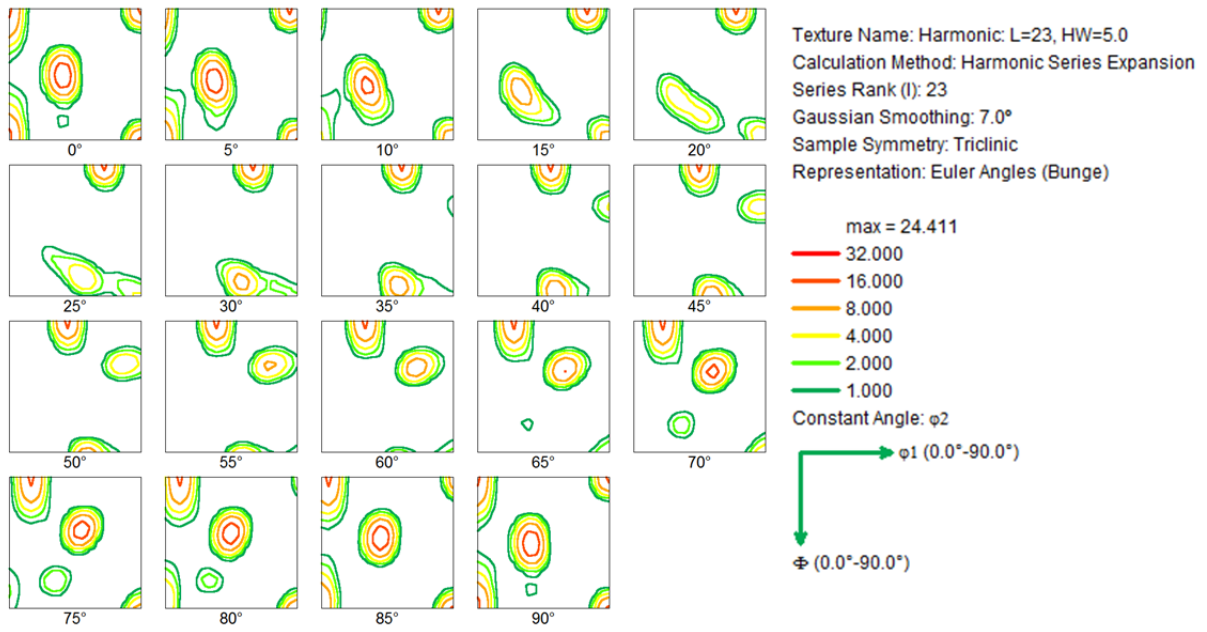
Figure 2: Orientation distribution function for the 6082.50 alloy.
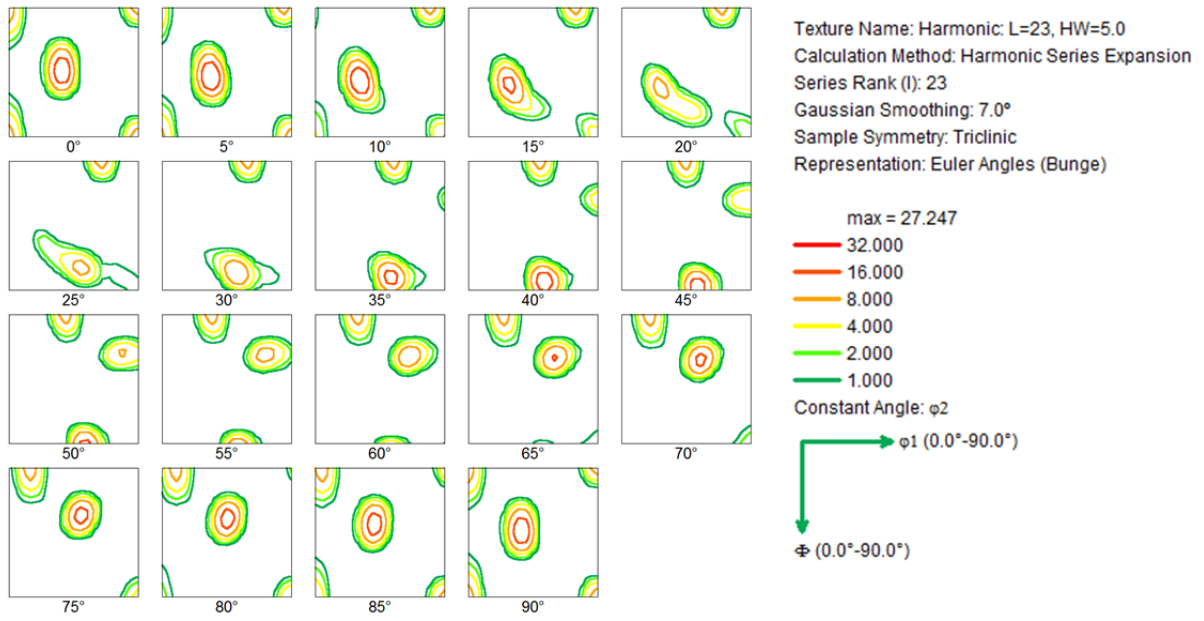
Figure 3: Orientation distribution function for the 6082.25 alloy.
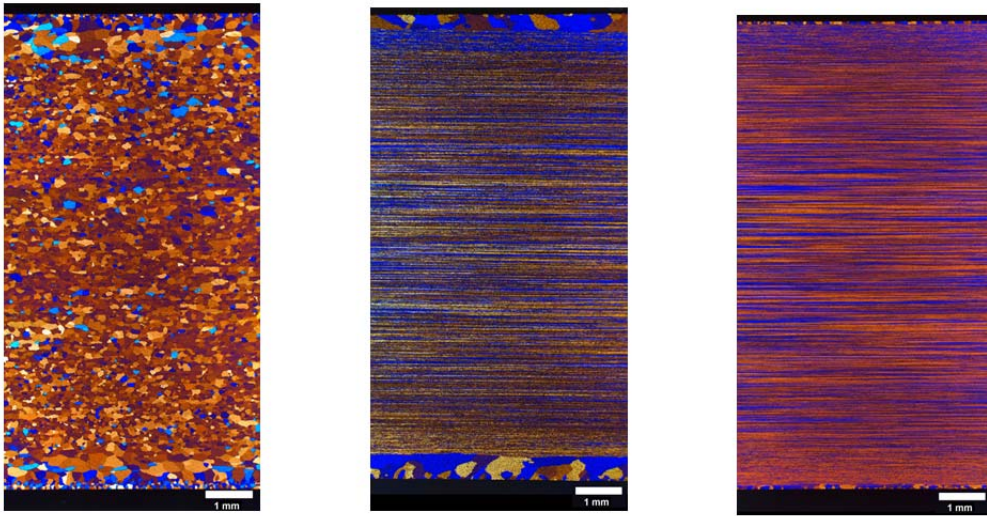
Figure 4: Grain structure of the 6060 (left), 6082.50 (centre) and 6082.25 (right) alloys, where the extrusion direction is horizontal and the normal (or thickness) direction is vertical.
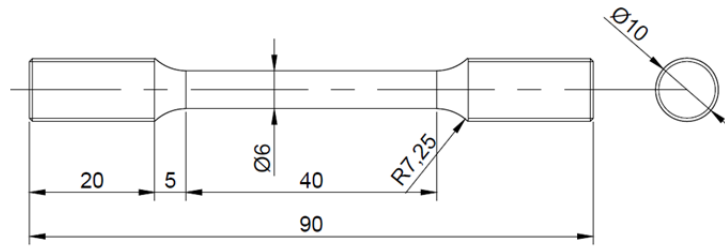
Figure 5: Tensile specimen geometry.
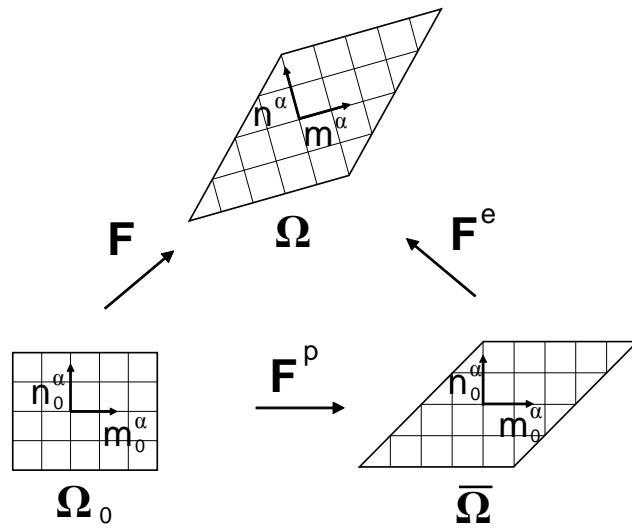
Figure 6: Decomposition of the total deformation gradient into elastic and plastic parts.
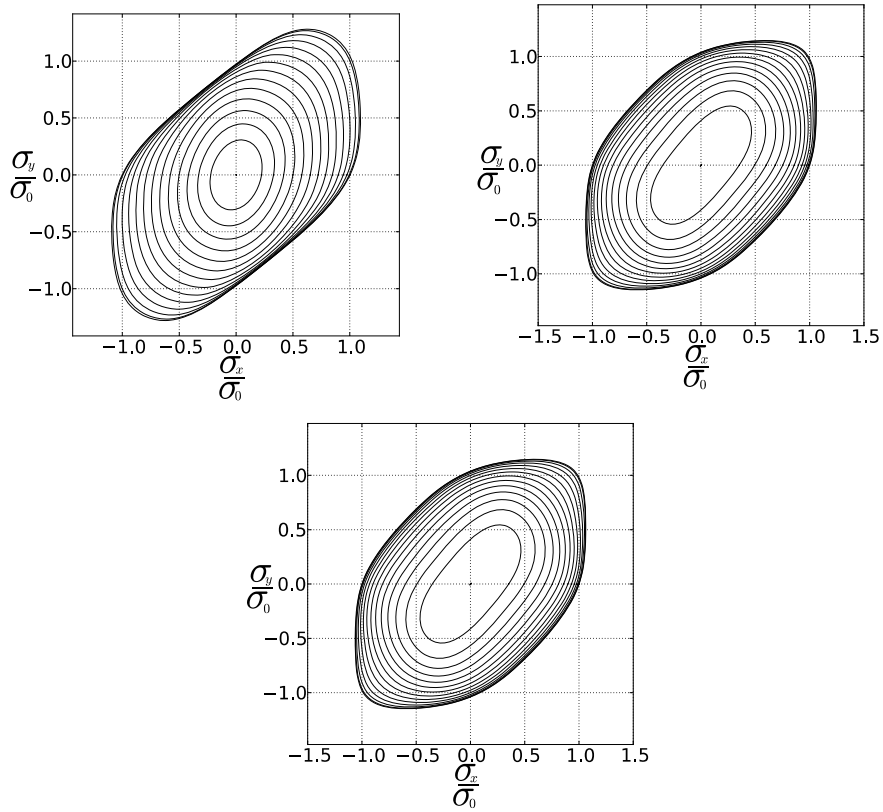
Figure 7: Generated yield surfaces for alloys 6060 (top left), 6082.50 (top right) and 6082.25 (bottom). Maximum value of σ_{xy} / σ_0 is 0.88 for 6060 and 0.52 for 6082 alloys.

Figure 8: Finite element mesh of the tensile specimen.
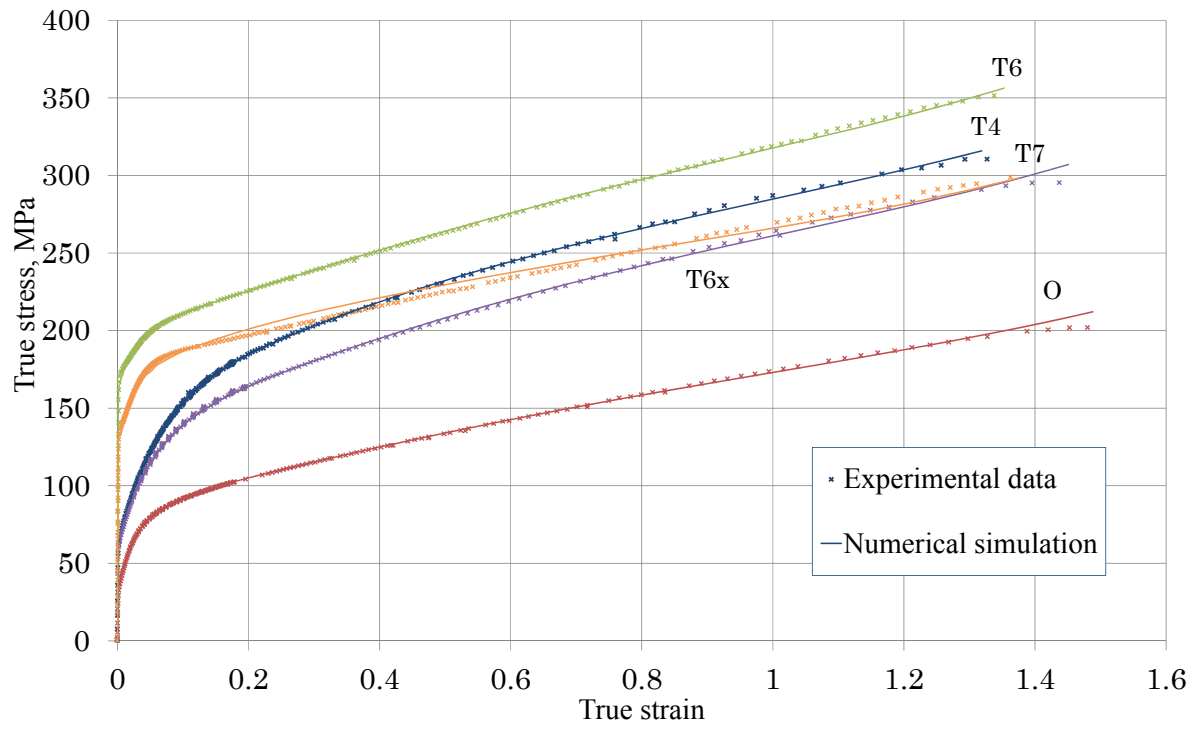
Figure 9: True stress versus logarithmic strain curve for the 6060 alloy.
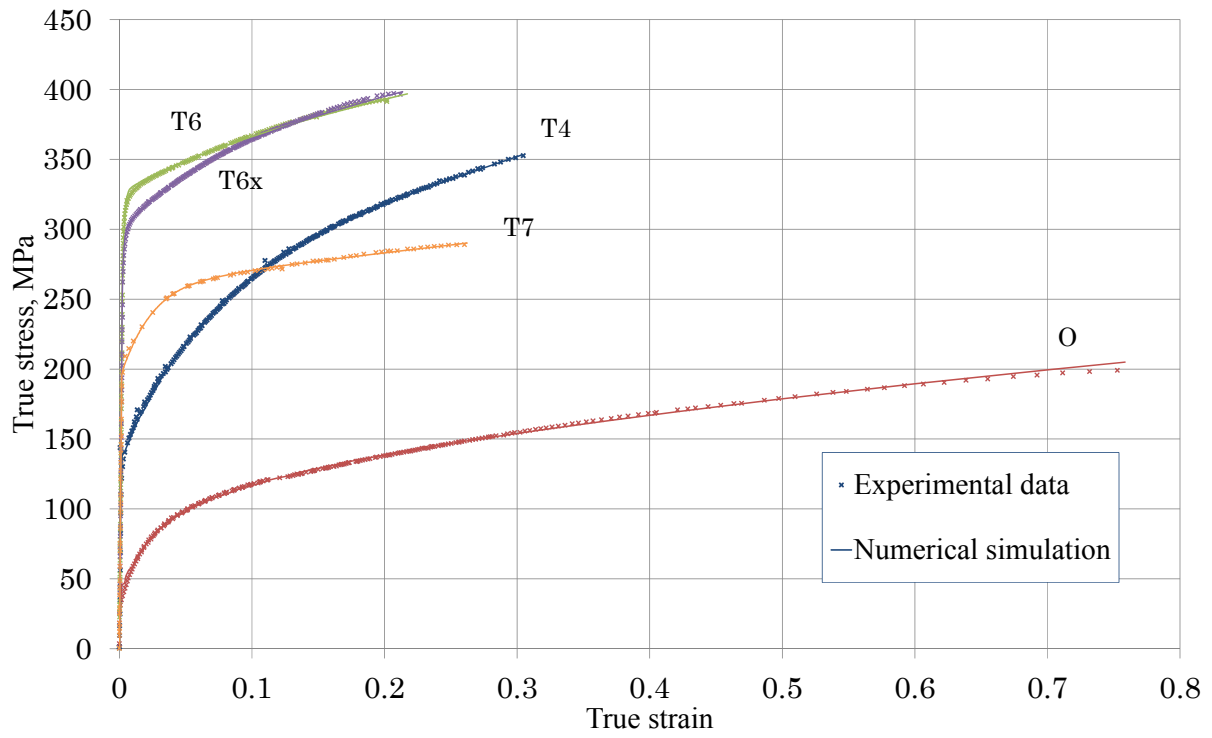
Figure 10: True stress versus logarithmic strain curve for the 6082.50 alloy.
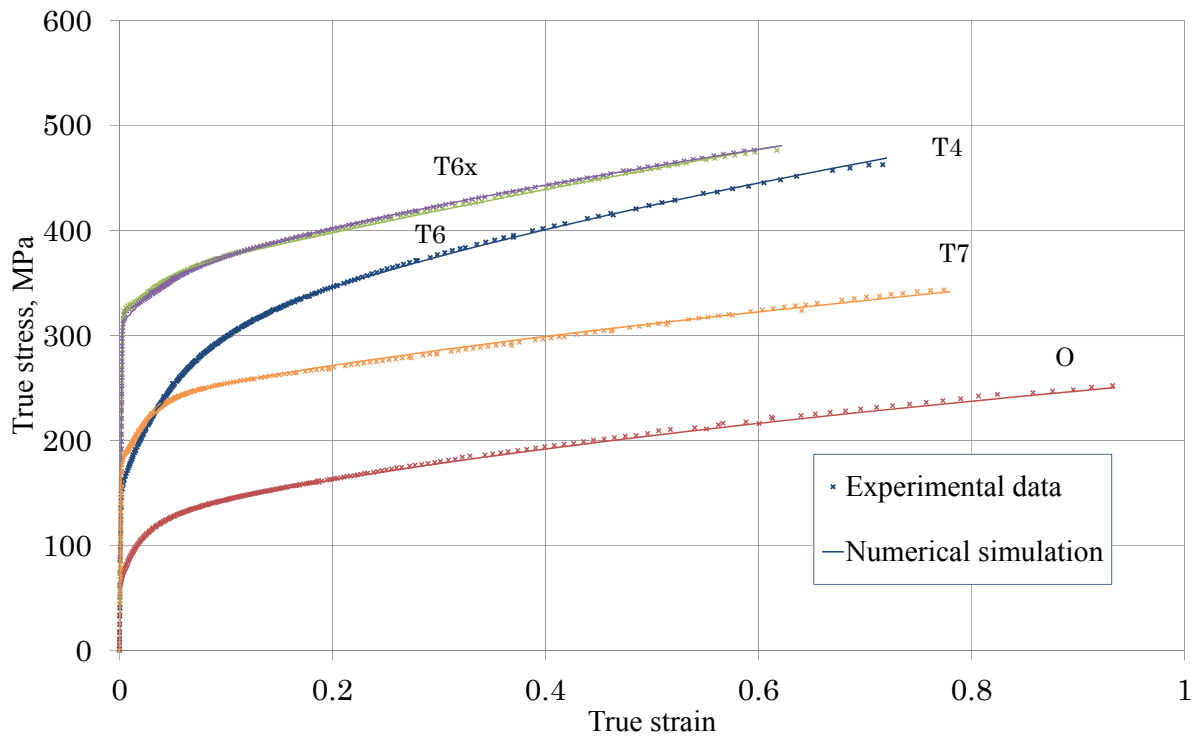
Figure 11: True stress versus logarithmic strain curve for the 6082.25 alloy.
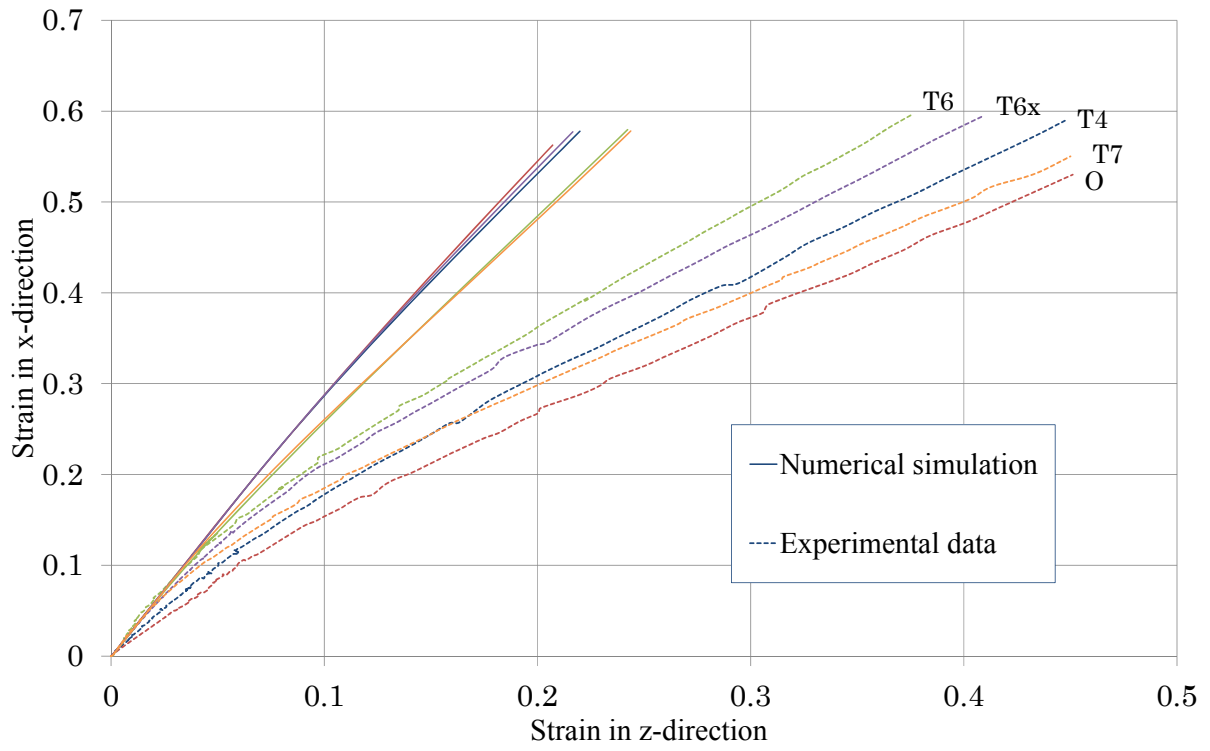
Figure 12: Logarithmic strain in extrusion direction (ε_x) versus logarithmic strain in normal direction (ε_z) for the 6060 alloy.
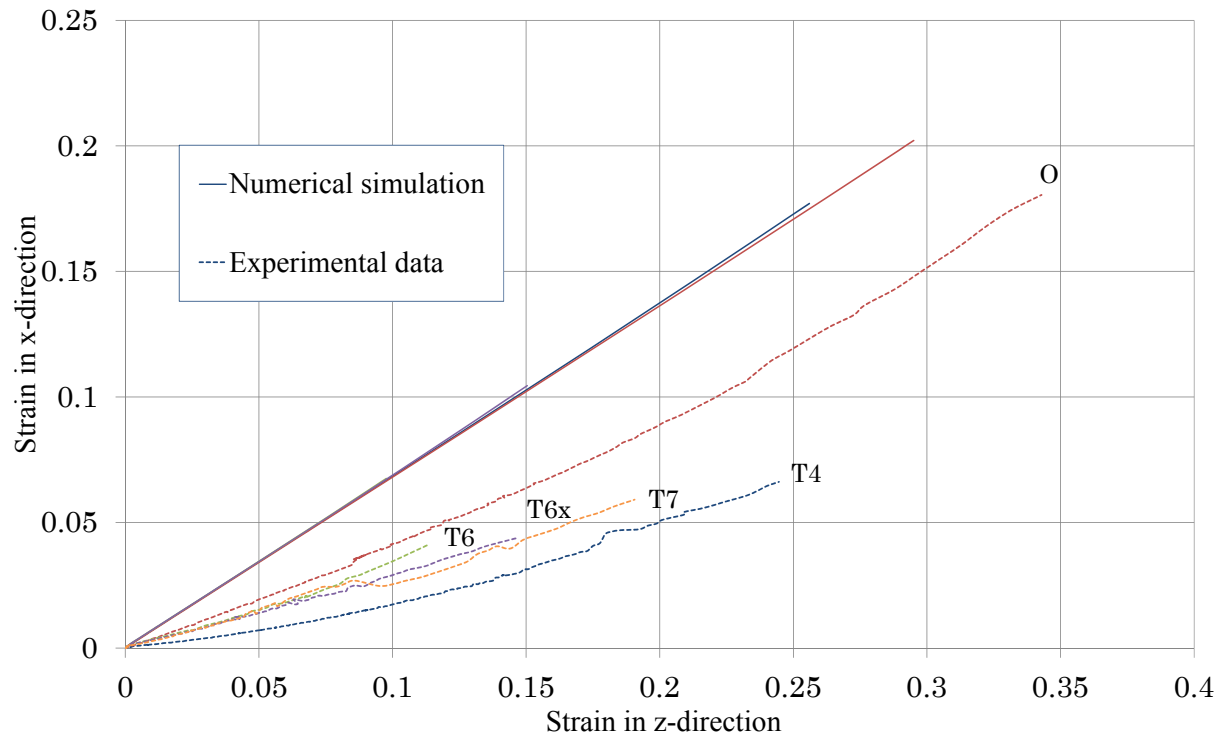
Figure 13: Logarithmic strain in extrusion direction (ε_x) versus logarithmic strain in normal direction (ε_z) for the 6082.50 alloy.
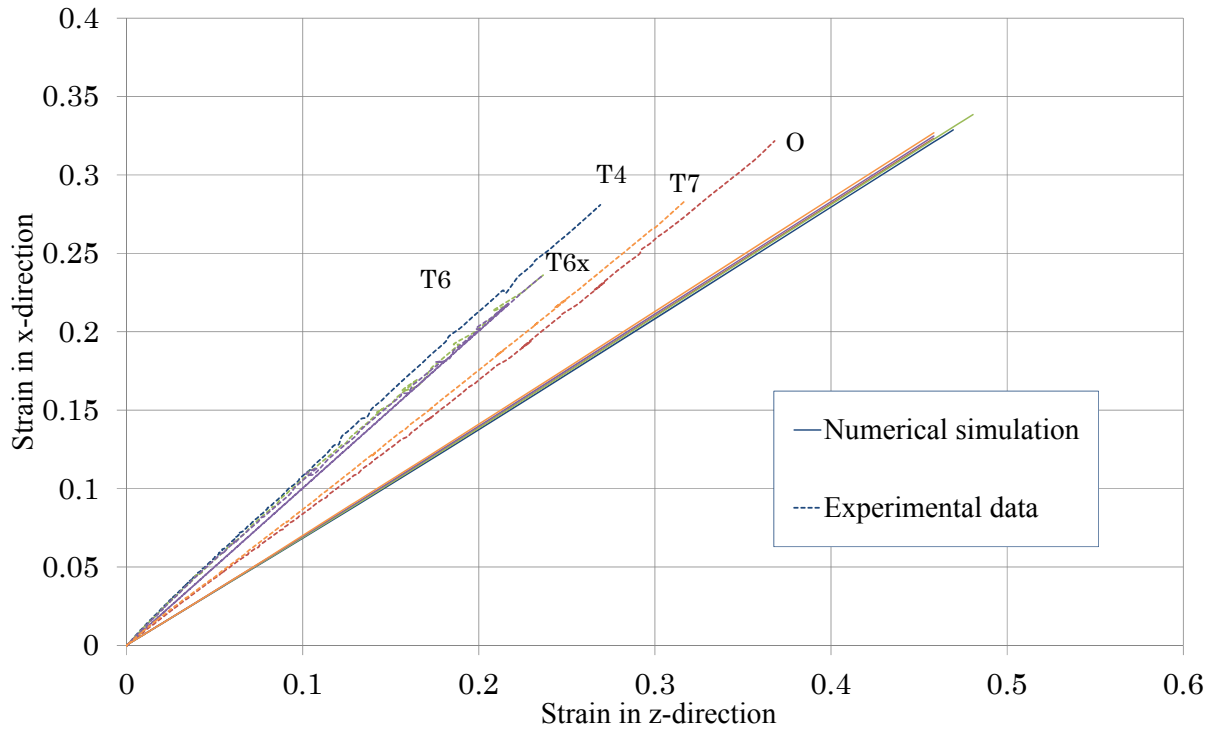
Figure 14: Logarithmic strain in extrusion direction (ε_x) versus logarithmic strain in normal direction (ε_z) for the 6082.25 alloy.

Figure 15: Necking in FEM model and real specimen in 6060-T4 (left) and 6082.25-T6x (right).
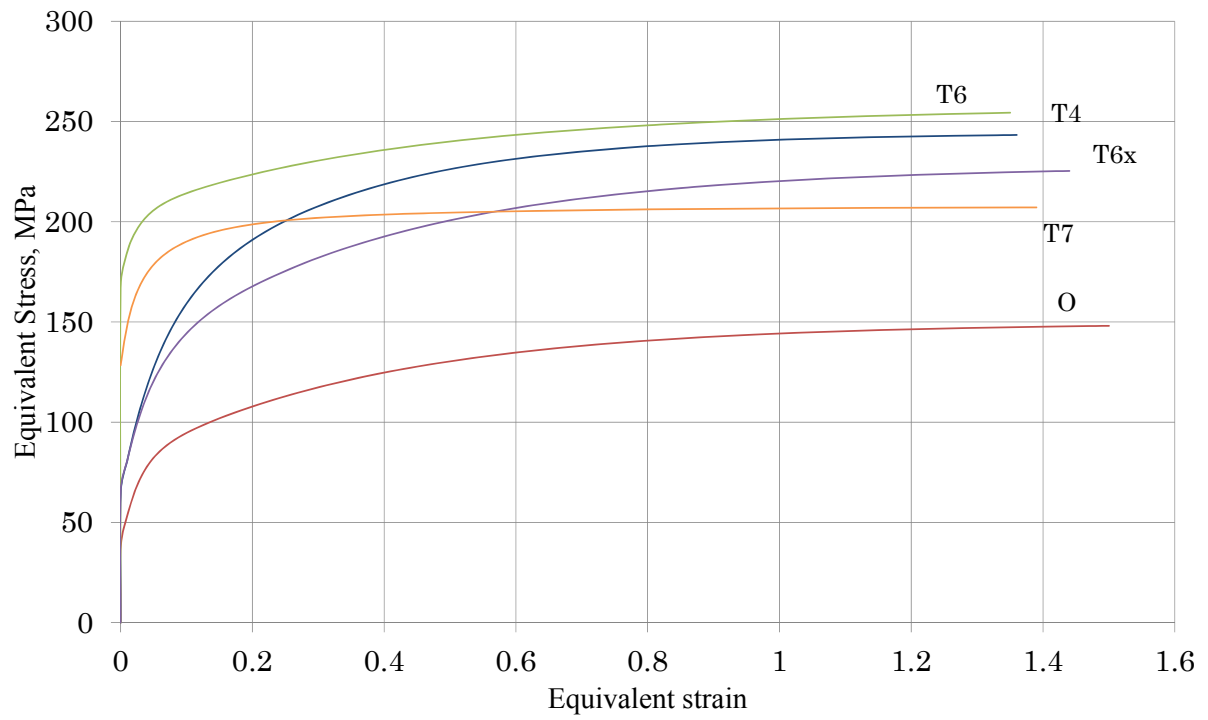
Figure 16: Equivalent stress-strain curves for the 6060 alloy.
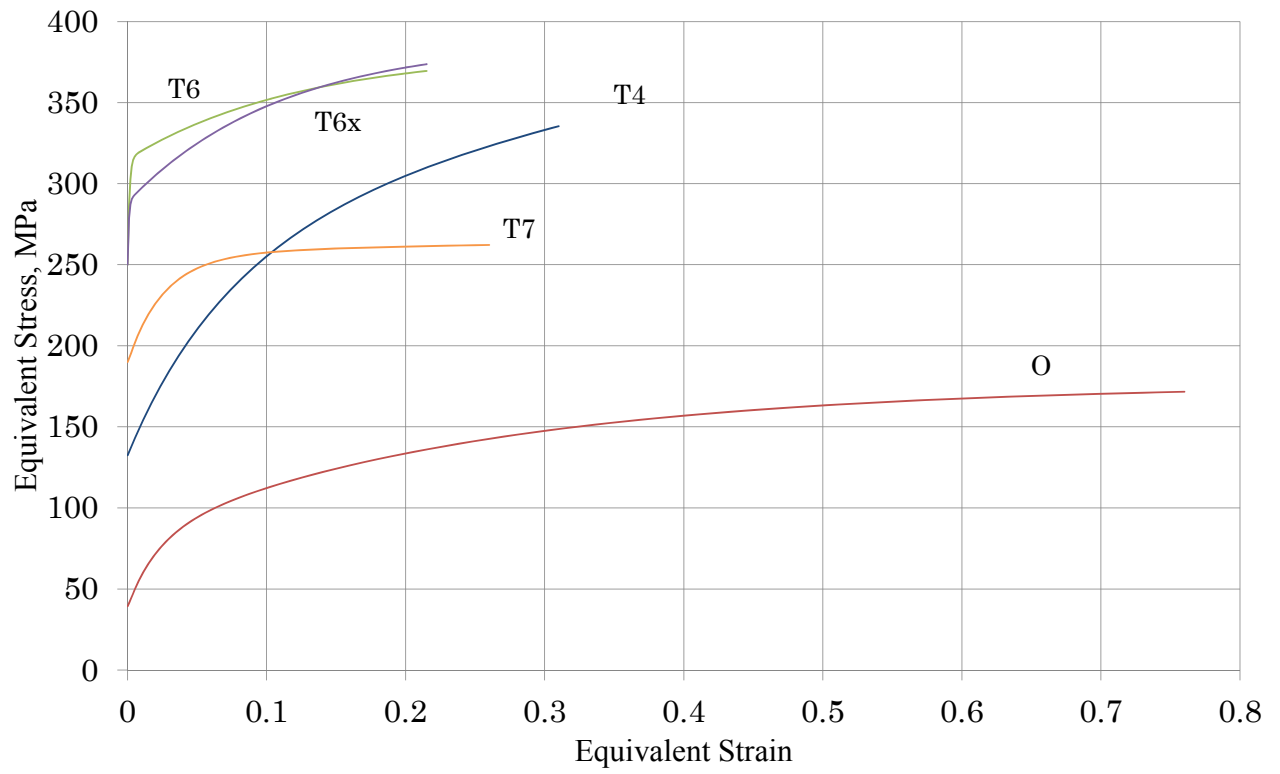
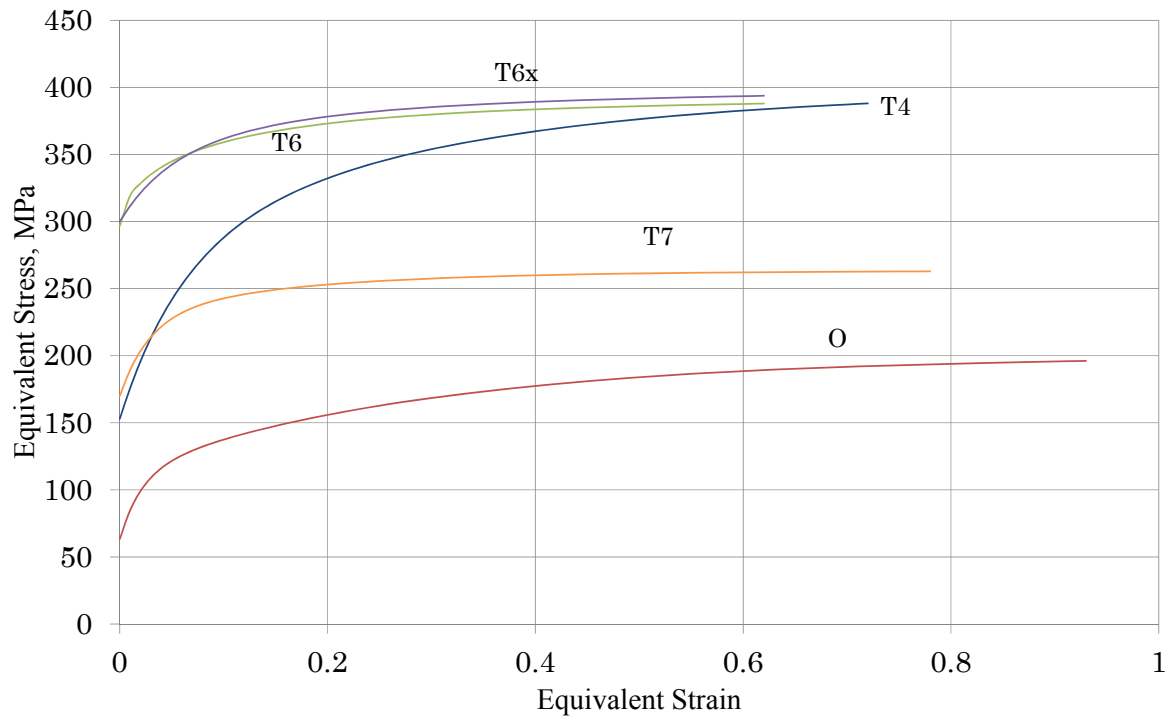Figure 17: Equivalent stress-strain curves for the 6082.50 alloy.

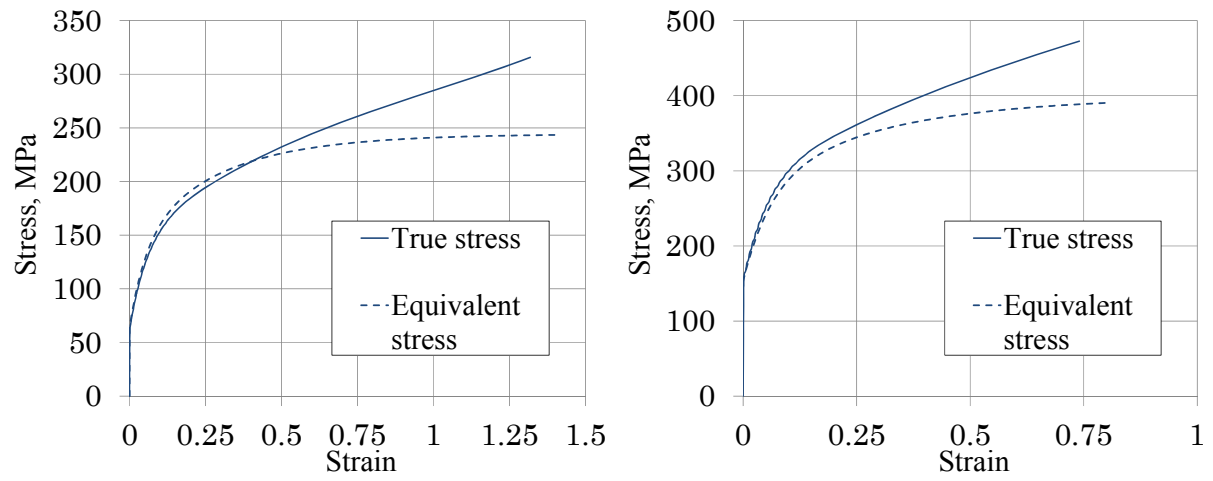Figure 18: Equivalent stress-strain curves for the 6082.25 alloy.

Figure 19: Comparison between equivalent and true stress versus logarithmic strain curves for 6060-T4 (left) and 6082.25-T4 (right).
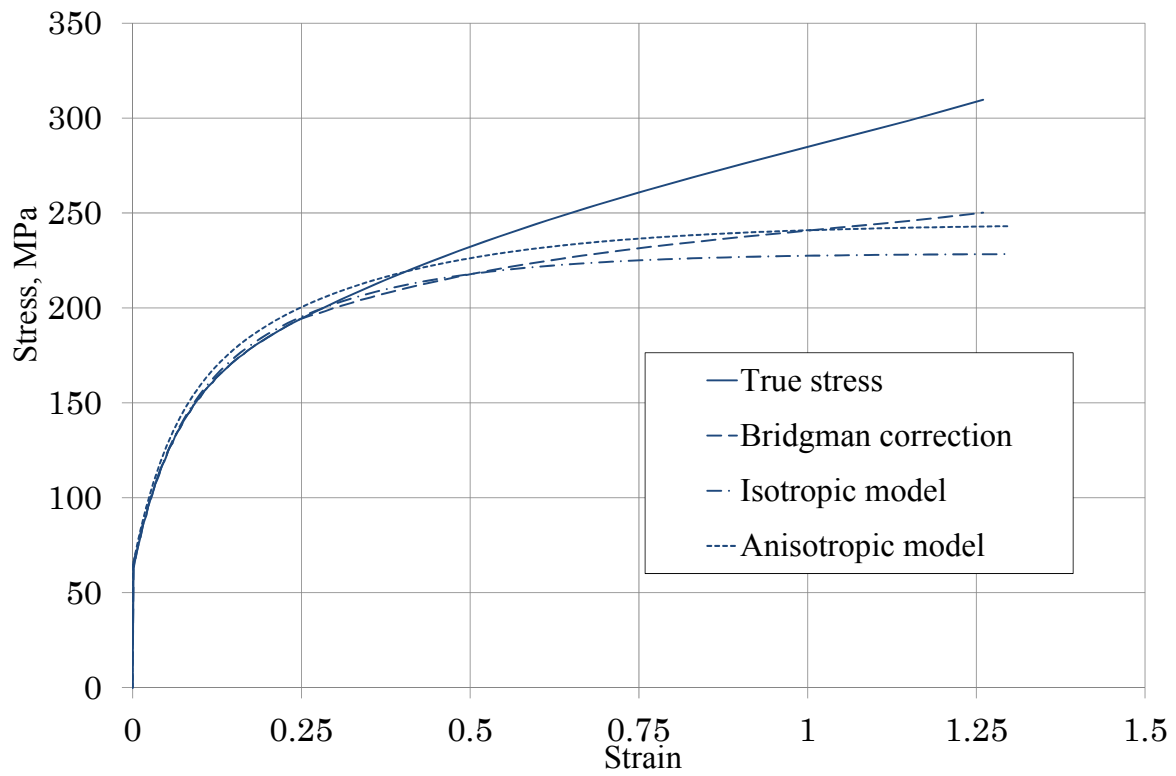
Figure 20: Comparison between different methods of estimating the equivalent stress-strain curve based on measured true stress-strain curve for the 6060 alloy in temper T4.